Supporting Information

Conformational dynamics and phase behavior of lipid vesicles in a precisely controlled extensional flow

Dinesh Kumar,[1, 2] Channing M. Richter,[1] and Charles M. Schroeder[1, 2, 3, *]

[1]*Department of Chemical and Biomolecular Engineering*
University of Illinois at Urbana-Champaign, Urbana, IL, 61801
[2]*Beckman Institute for Advanced Science and Technology*
University of Illinois at Urbana-Champaign, Urbana, IL, 61801
[3]*Department of Materials Science and Engineering*
University of Illinois at Urbana-Champaign, Urbana, IL, 61801
(Dated: November 17, 2019)

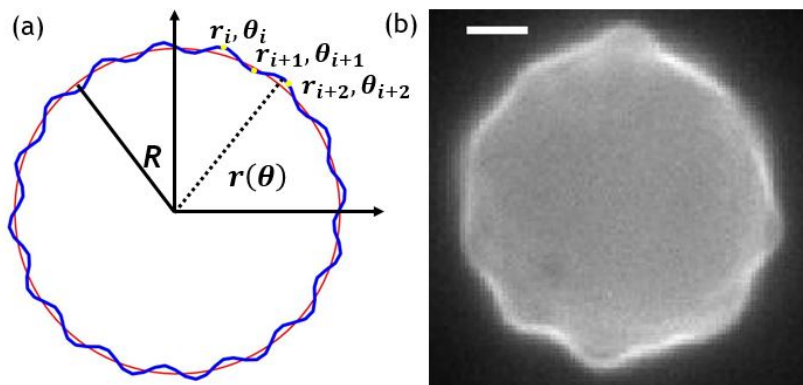* To whom correspondence must be addressed: cms@illinois.edu

FIG. S1. Determination of bending modulus. (a) Schematic of a quasi-spherical vesicle in the focal plane of the microscope showing the Fourier modes of the membrane. (b) Image of a quasi-spherical vesicle with fluctuation modes captured by fluorescence microscopy. Scale bar: 5 μm.

I.   BENDING MODULUS DETERMINATION

A.   Edge detection of vesicle

We began by determining the bending modulus of lipid vesicles at equilibrium (no flow conditions), which requires accurate detection of the membrane. In the following, we describe the procedure of 'edge' detection for identifying the location of the fluctuating membrane of a freely suspended vesicle. Fig. S1(a) shows a schematic of a fluctuating contour of a vesicle membrane. Fig. S1(b) shows an experimental image with fluctuating membrane modes captured using fluorescence microscopy. In order to accurately determine the bending modulus of DOPC vesicles, we perform the following steps to precisely detect the position of membrane (r_i, θ_i) and recreate the full contour.

1. For each frame of a 30 s movie of vesicle fluctuations at equilibrium (acquired at a frame rate of 30 Hz), we apply Gaussian smoothing around the vesicle edges to minimize experimental noise that may inhibit the boundary detection method.

2. Image thresholding is performed, followed by transforming the image array into a checkerboard pattern, after which the diagonal and off-diagonal elements of the original image array are converted into new subsections of rectangular arrays. Instead of searching for pixels with maximum intensity values only along the rows (x axis) and columns (y axis) of the original image array (which may result in image intensity artifacts in the region where edge is not close to either x and y axis), the algorithm instead searches along the rows (($\bar{x}$) axis), and columns (($\bar{y}$) axis) of three different views, namely the original image array transformed rectangular arrays of diagonal elements and off-diagonal element to locate the coordinates of pixels having maximum intensity value. This provides pixel-level resolution of vesicle edges in each view.

3. The location of the membrane edges are determined with sub-pixel resolution using the method of weighted regression over all views, as described in prior work [1]. For all determined contour coordinate points, we use a Delaunay triangulation method [2] to find all nearest neighbors and form a cluster. A minimum spanning tree algorithm is then applied to identify complete loops that are candidates for potential contours without artefacts, and all the extra points are de-noised using Savitzky-Golay filter to obtain a smooth contour profile.

4. Steps 1-3 are repeated for each frame of the movie and coordinate position of the membrane are stored as a structure in MATLAB defining the edge location in space and time.

B.   Mode number dependence of bending modulus

The amplitude of fluctuations from the Helfrich model $\left\langle |u_H(q_x)|^2 \right\rangle$ (Eq. 6 in main text) has been corrected to account for the finite integration time of camera. Nevertheless, the spatial resolution of the camera and imaging system generally inhibits analysis for large values of the wavenumber, q_x. In this way, the bending modulus obtained

from the shape fluctuation analysis is sensitive to the number of modes chosen in the fit.

For these reasons, the first five modes ($n = $ 1-5) are not included in the fitting procedure to conform with the planar membrane analysis of fluctuating vesicles as discussed in detail in prior work [3]. For the bending modulus measurements in our experiments, we generally see that κ_b is roughly independent of mode number in the range $n = $ 6-25. On fitting mode numbers larger than 25, we observe that the mean-square amplitude fluctuations are corrupted by noise, and hence these modes are not considered in the fitting procedure. The optimal range of $n = $ 6-25 gives us a mean value of κ_b which is in the bending regime, consistent with prior works [4, 5].

II. DETERMINING UNCERTAINTY IN BENDING MODULUS

To estimate the coupling between κ_b and σ values obtained from fitting as described in Section 2.4.2 (main text) , we calculate the correlation coefficient $corr(\sigma, \kappa_b)$. As noted in the main text, $corr(\sigma, \kappa_b)$ is one of the criterion for vesicle exclusion that is too tense to give us an accurate estimate of bending modulus.

We began by calculating the standard deviation of every measured quantity in the fluctuation analysis method. Briefly, we assume that the uncertainty in determining the position (x_i, y_i) of a coordinate point on the vesicle contour is normally distributed with a zero mean and standard deviation σ_0. Following prior work [3], we then determine the standard deviation of polar coordinates (r_i, θ_i) and the corresponding covariances as:

$$\sigma_{r_i} = \sqrt{2}\sigma_0 \tag{S1}$$

$$\sigma_{\theta_i} = \frac{\sqrt{2}\sigma_0}{r_i} \tag{S2}$$

$$\sigma_{r_i\theta_j}^2 = cov\left(r_i, \theta_j\right) = \delta_{ij}\frac{2\sigma_0^2}{r_i} \tag{S3}$$

Next, the uncertainty in the contour radius R and Fourier amplitudes a_n, b_n and c_n are determined. The error is propagated using the chain rule of differentiation, as described in Philip and Bevington [6]. For a derived quantity $x_1 = h(u, v)$ that depends on independent variables u and v, the variance of x_1 is given by:

$$\sigma_{x_1}^2 = \left(\frac{\partial x_1}{\partial u}\right)^2 \sigma_u^2 + \left(\frac{\partial x_2}{\partial v}\right)^2 \sigma_v^2 + 2\frac{\partial x_1}{\partial u}\frac{\partial x_2}{\partial v}\sigma_{uv}^2 \tag{S4}$$

For our analysis, all derived quantities (including contour radius R, Fourier amplitudes a_n, b_n, c_n, and fluctuation amplitude $\left\langle |u\left(q_x\right)|^2\right\rangle$) depend on the independent variables (r_i, θ_i). The relevant derivatives are given as follows:

$$\frac{\partial R}{\partial r_i} = \frac{1}{4\pi}\left(\theta_{i+1} - \theta_{i-1}\right) \tag{S5}$$

$$\frac{\partial R}{\partial \theta_i} = \frac{1}{4\pi}\left(r_{i-1} - r_{i+1}\right) \tag{S6}$$

$$\frac{\partial a_n}{\partial R} = \frac{-a_n}{R}; \qquad \frac{\partial a_n}{\partial r_i} = \frac{1}{\pi R}\cos n\theta_i \frac{\left(\theta_{i+1} - \theta_{i-1}\right)}{2} \tag{S7}$$

$$\frac{\partial a_n}{\partial \theta_i} = \frac{1}{\pi R}\left[-r_i n \sin\left(n\theta_i\right)\frac{\theta_{i+1} - \theta_{i-1}}{2} - \frac{r_{i+1}\cos n\theta_{i+1} - r_{i-1}\cos n\theta_{i-1}}{2}\right] \tag{S8}$$

$$cov\left(r_i, R\right) = \frac{2\sigma_0^2}{4\pi}\left(\theta_{i+1} - \theta_{i-1} + \frac{r_{i-1} - r_{i+1}}{r_i}\right) \tag{S9}$$

$$cov\left(\theta_i, R\right) = \frac{2\sigma_0^2}{4\pi r_i}\left(\theta_{i+1} - \theta_{i-1} + \frac{r_{i-1} - r_{i+1}}{r_i}\right) \tag{S10}$$

From these quantities, we then compute the variances and covariance as follows:

$$\sigma_R^2 = \sum_{i=1}^{N}\left(\frac{\theta_{i+1} - \theta_{i-1}}{4\pi}\right)^2 2\sigma_0^2 + \left(\frac{r_{i-1} - r_{i+1}}{4\pi}\right)^2 \frac{2\sigma_0^2}{r_i^2} + \frac{2\left(r_{i-1} - r_{i+1}\right)\left(\theta_i - \theta_{i-1}\right)}{4\pi}\frac{2\sigma_0^2}{r_i} \tag{S11}$$

$$\sigma_{a_n}^2 = \sigma_R^2\left(\frac{a_n}{R}\right)^2 + \sum_{i=1}^{N}\sigma_0^2\left(\frac{1}{\pi R}\right)^2 \frac{\cos^2 n\theta_i}{2}\left(\theta_{i+1} - \theta_{i-1}\right)^2$$

$$+ \sum_{i=1}^{N}\frac{2\sigma_0^2}{r_i}\left(\frac{1}{\pi R}\right)^2\left[-r_i n\sin\left(n\theta_i\right)\frac{\theta_{i+1} - \theta_{i-1}}{2} - \frac{r_{i+1}\cos n\theta_{i+1} - r_{i-1}\cos n\theta_{i-1}}{2}\right]^2$$

$$+ 2\sum_{i=1}^{N}\frac{\sigma_0^2}{4\pi}\left[\theta_{i+1} - \theta_{i-1} + \frac{r_{i-1} - r_{i+1}}{r_i}\right]\left(\frac{-a_n}{R}\right)\frac{1}{\pi R}\cos n\theta_i\left(\theta_{i+1} - \theta_{i-1}\right)$$

$$+ 2\sum_{i=1}^{N}\frac{\sigma_0^2}{4\pi r_i}\left[\theta_{i+1} - \theta_{i-1} + \frac{r_{i-1} - r_{i+1}}{r_i}\right]\left(\frac{-a_n}{R}\right)\frac{1}{\pi R}\left[-r_i n\sin\left(n\theta_i\right)\frac{\theta_{i+1} - \theta_{i-1}}{2} - \frac{r_{i+1}\cos n\theta_{i+1} - r_{i-1}\cos n\theta_{i-1}}{2}\right]$$

$$+ 2\sum_{i=1}^{N}\frac{2\sigma_0^2}{r_i}\left(\frac{1}{\pi R}\right)^2 \frac{\cos n\theta_i}{2}\left(\theta_{i+1} - \theta_{i-1}\right)\left[-r_i n\sin n\theta_i\frac{\theta_{i+1} - \theta_{i-1}}{2} - \frac{r_{i+1}\cos n\theta_{i+1} - r_{i-1}\cos n\theta_{i-1}}{2}\right] \tag{S12}$$

$$\sigma_{b_n}^2 = \sigma_R^2\left(\frac{b_n}{R}\right)^2 + \sum_{i=1}^{N}\sigma_0^2\left(\frac{1}{\pi R}\right)^2 \frac{\sin^2 n\theta_i}{2}\left(\theta_{i+1} - \theta_{i-1}\right)^2$$

$$+ \sum_{i=1}^{N}\frac{2\sigma_0^2}{r_i}\left(\frac{1}{\pi R}\right)^2\left[r_i n\cos\left(n\theta_i\right)\frac{\theta_{i+1} - \theta_{i-1}}{2} - \frac{r_{i+1}\sin n\theta_{i+1} - r_{i-1}\sin n\theta_{i-1}}{2}\right]^2$$

$$+ 2\sum_{i=1}^{N}\frac{\sigma_0^2}{4\pi}\left[\theta_{i+1} - \theta_{i-1} + \frac{r_{i-1} - r_{i+1}}{r_i}\right]\left(\frac{-b_n}{R}\right)\frac{1}{\pi R}\sin n\theta_i\left(\theta_{i+1} - \theta_{i-1}\right)$$

$$+ 2\sum_{i=1}^{N}\frac{\sigma_0^2}{4\pi r_i}\left[\theta_{i+1} - \theta_{i-1} + \frac{r_{i-1} - r_{i+1}}{r_i}\right]\left(\frac{-b_n}{R}\right)\frac{1}{\pi R}\left[r_i n\cos\left(n\theta_i\right)\frac{\theta_{i+1} - \theta_{i-1}}{2} - \frac{r_{i+1}\sin n\theta_{i+1} - r_{i-1}\sin n\theta_{i-1}}{2}\right]$$

$$+ 2\sum_{i=1}^{N}\frac{2\sigma_0^2}{r_i}\left(\frac{1}{\pi R}\right)^2 \frac{\sin n\theta_i}{2}\left(\theta_{i+1} - \theta_{i-1}\right)\left[r_i n\cos n\theta_i\frac{\theta_{i+1} - \theta_{i-1}}{2} - \frac{r_{i+1}\sin n\theta_{i+1} - r_{i-1}\sin n\theta_{i-1}}{2}\right] \tag{S13}$$

$$cov\left(a_n, R\right) = \left(\frac{a_n}{R}\right)^2\sigma_R^2 + \sum_{i=1}^{N}\left[\frac{1}{\pi R}\cos n\theta_i\frac{\left(\theta_{i+1} - \theta_{i-1}\right)}{2}\frac{2\sigma_0^2}{4\pi}\left(\theta_{i+1} - \theta_{i-1} + \frac{r_{i-1} - r_{i+1}}{r_i}\right)\right]$$

$$+ \sum_{i=1}^{N}\frac{1}{\pi R}\left(-r_i n\sin n\theta_i\frac{\theta_{i+1} - \theta_{i-1}}{2} - \frac{r_{i+1}\cos n\theta_{i+1} - r_{i-1}\cos n\theta_{i-1}}{2}\right)\frac{2\sigma_0^2}{4\pi r_i}\left(\theta_{i+1} - \theta_{i-1} + \frac{r_{i-1} - r_{i+1}}{r_i}\right) \tag{S14}$$

$$cov\left(b_{n}, R\right) = \left(\frac{b_{n}}{R}\right)^{2} \sigma_{R}^{2} + \sum_{i=1}^{N} \left[\frac{1}{\pi R} \sin n\theta_{i} \frac{(\theta_{i+1} - \theta_{i-1})}{2} \frac{2\sigma_{0}^{2}}{4\pi} \left(\theta_{i+1} - \theta_{i-1} + \frac{r_{i-1} - r_{i+1}}{r_{i}}\right)\right]$$

$$+ \sum_{i=1}^{N} \frac{1}{\pi R} \left(r_{i}n \cos n\theta_{i} \frac{\theta_{i+1} - \theta_{i-1}}{2} - \frac{r_{i+1} \sin n\theta_{i+1} - r_{i-1} \sin n\theta_{i-1}}{2}\right) \frac{2\sigma_{0}^{2}}{4\pi r_{i}} \left(\theta_{i+1} - \theta_{i-1} + \frac{r_{i-1} - r_{i+1}}{r_{i}}\right)$$

(S15)

$$cov\left(a_{n}, b_{n}\right) = \frac{cov\left(a_{n}, R\right) cov\left(b_{n}, R\right)}{\sigma_{R}^{2}} \tag{S16}$$

Using the relations $c_{n} = \sqrt{a_{n}^{2} + b_{n}^{2}}$ and $q_{x} = \frac{n}{\langle R \rangle}$, we similarly calculate $\sigma_{\langle c_{n} \rangle}^{2}$, $\sigma_{\langle c_{n}^{2} \rangle}^{2}$ and $\sigma_{q_{x}}^{2}$. Taking into account the time average over N contours of each vesicle, we also compute the variances and covariances for average quantities of $\langle R \rangle$, $\langle c_{n} \rangle$, $\langle c_{n}^{2} \rangle$. If j is the index over the number of contours:

$$\sigma_{\langle R \rangle}^{2} = \frac{1}{N^{2}} \sum_{j=1}^{N} \sigma_{R}^{2} \tag{S17}$$

Similar results can be written for other quantities. Next, we determine the quantities:

$$\sigma_{q_{x}}^{2} = \frac{n^{2}}{(\langle R \rangle)^{4}} \sigma_{\langle R \rangle}^{2} \tag{S18}$$

$$\sigma_{\langle |u(q_{x})|^{2} \rangle}^{2} = \left(\frac{\pi}{2} \langle R \rangle^{3}\right)^{2} \sigma_{\langle c_{n}^{2} \rangle}^{2} + \left(\frac{\pi}{2} \langle R \rangle^{3}\right)^{2} (2 \langle c_{n} \rangle)^{2} \sigma_{\langle c_{n} \rangle}^{2} + \left(\frac{3\pi}{2} \langle R \rangle^{2} \left(\langle c_{n}^{2} \rangle - \langle c_{n} \rangle^{2}\right)\right)^{2} \sigma_{\langle R \rangle}^{2}$$

$$- 4 \langle c_{n} \rangle \left(\frac{\pi}{2} \langle R \rangle^{3}\right)^{2} cov\left(\langle c_{n}^{2} \rangle, \langle c_{n} \rangle\right) + \langle R \rangle^{3} \left(\langle c_{n}^{2} \rangle - \langle c_{n} \rangle^{2}\right) \frac{3\pi^{2}}{2} \langle R \rangle^{2} cov\left(\langle c_{n}^{2} \rangle, \langle R \rangle\right)$$

$$- 3 \langle c_{n} \rangle \pi^{2} \langle R \rangle^{3} \left(\langle c_{n}^{2} \rangle - \langle c_{n} \rangle^{2}\right) \langle R \rangle^{2} cov\left(\langle c_{n} \rangle, \langle R \rangle\right)$$

(S19)

Following prior work [3], we can directly write the standard deviation and covariance of κ_{b} and σ as follows:

$$\sigma_{\sigma}^{2} = \frac{\hat{K}}{|W|} \sum_{k} \left(\frac{\partial f}{\partial \kappa_{b}}\right)^{2} g_{k} \tag{S20}$$

$$\sigma_{\kappa_{b}}^{2} = \frac{\hat{K}}{|W|} \sum_{k} \left(\frac{\partial f}{\partial \sigma}\right)^{2} g_{k} \tag{S21}$$

$$cov\left(\sigma, \kappa_{b}\right) = \frac{\hat{K}}{|W|} \sum_{k} \left(\frac{\partial f}{\partial \sigma} \frac{\partial f}{\partial \kappa_{b}}\right) g_{k} \tag{S22}$$

where k is the new index of Fourier modes (k=6-25), and f describes the theoretical fluctuation amplitudes (eqn. 6 in the main text) from the Helfrich model such that :

$$f\left(\kappa_{b}, \sigma, q_{x}\right) \equiv \left\langle |u_{H}\left(q_{x}\right)|^{2} \right\rangle = \frac{1}{\pi} \int_{-\infty}^{\infty} \frac{kT}{4\mu_{out}q_{\perp}} \tau_{m} \frac{\tau_{m}^{2}}{\tau^{2}} \left[\frac{\tau}{\tau_{m}} + \exp\left(\frac{-\tau}{\tau_{m}}\right) - 1\right] dq_{y}$$

Then, the quantities g_{k}, $\hat{K}$, and $|W|$ are expressed as:

$$g_k = \frac{1}{\sigma^2_{\langle |u(q_x)|^2 \rangle} + \left(\frac{\partial f}{\partial q_x} \right)^2 \sigma^2_{q_x}} \tag{S23}$$

$$\hat{K} = \frac{1}{P-2} \sum_{k=1}^{P} g_k \left[\left\langle |u(q_x)|^2 \right\rangle - f(q_x, \sigma, \kappa_b) \right]^2 \tag{S24}$$

$$W = \begin{bmatrix} \sum_k \left(\frac{\partial f}{\partial \sigma} \right)^2 g_k & \sum_k \frac{\partial f}{\partial \sigma} \frac{\partial f}{\partial \kappa_b} g_k \\ \sum_k \frac{\partial f}{\partial \sigma} \frac{\partial f}{\partial \kappa_b} g_k & \sum_k \left(\frac{\partial f}{\partial \kappa_b} \right)^2 g_k \end{bmatrix} \tag{S25}$$

The central difference method is used to numerically compute the derivatives of f. Finally, we define the correlation coefficient of bending modulus and membrane tension as follows:

$$corr(\sigma, \kappa_b) = \frac{cov(\sigma, \kappa_b)}{\sigma_\sigma \sigma_{\kappa_b}} \tag{S26}$$

These equations are used to report the standard deviation in bending modulus and membrane tension listed in main text. Finally, the weighted mean of the bending modulus over a sample of M' vesicles is written as:

$$\bar{\kappa}_b = \frac{\sum_{i=1}^{M'} \frac{\kappa_{b,i}}{\sigma^2_{\kappa_{b,i}}}}{\sum_{i=1}^{M'} \frac{1}{\sigma^2_{\kappa_{b,i}}}} \tag{S27}$$

The uncertainty on this mean value of bending modulus is calculated as:

$$\sigma^2_{\bar{\kappa}_b} = \frac{1}{\sum_{1}^{M'} \frac{1}{\sigma^2_{\kappa_{b,i}}}} \tag{S28}$$

III.   REDUCED VOLUME CALCULATION

In this work, vesicles are imaged using epifluorescence microscopy, which results in a 2D image of the vesicle contour in the x-y plane. As discussed in the main text, vesicle contours are not always symmetric, so we divide the vesicle boundary into two halves as shown in Fig. S2. Edge detection of vesicles is performed using the same image analysis code for thermal fluctuation analysis as shown in Fig. S2. The detected vesicle contours in both halves are independently revolved along the short axis of vesicle, and numerical integration is used to calculate the surface area and volume of revolution of each half [7, 8]. Finally, the surface area and volume of the vesicle in each frame are taken to be the average of top and bottom half, with the uncertainty being equal to half the value for the respective halves. The error bars for the surface area and volume in Fig. S3 are calculated by propagation of error using Eq. S4 using a similar method for the bending modulus calculation. Lastly, the reduced volume of the vesicle is calculated for 100 frames as shown in Fig. S4 and the uncertainty weighted mean value over all frames is taken as the final value.
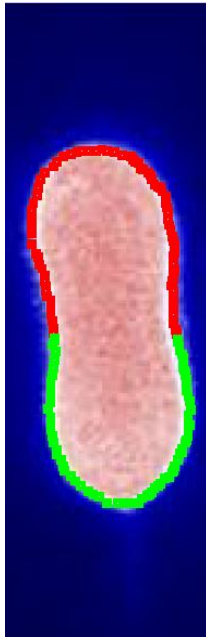
FIG. S2. Detected contour of a vesicle using image processing. The vesicle contour is divided into two halves for determination of reduced volume.
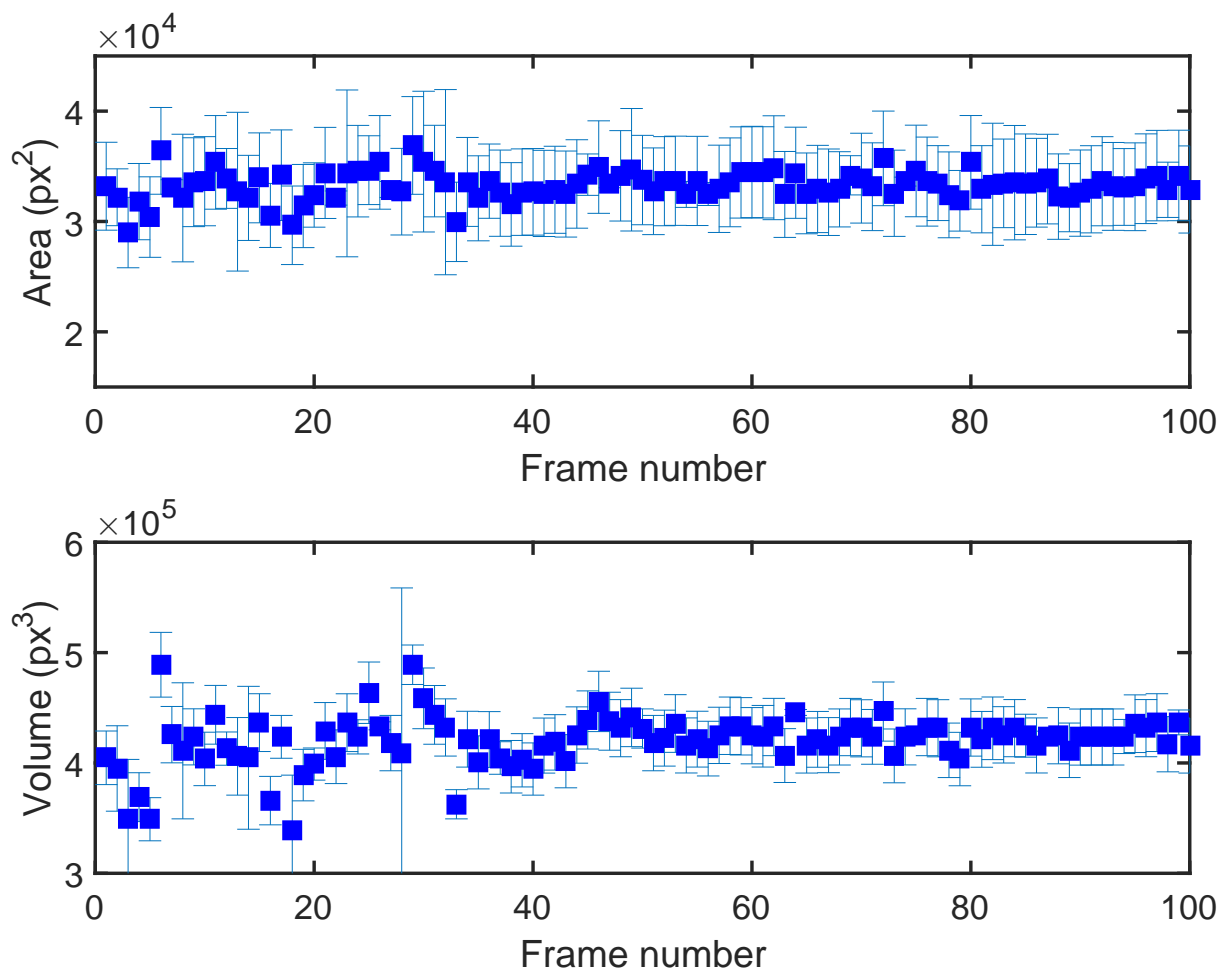
FIG. S3. Vesicle surface area and volume as a function of frame number for the vesicle shown in Fig. S2. Each individual data point for surface area and volume is taken as the average of measurements from the two halves.
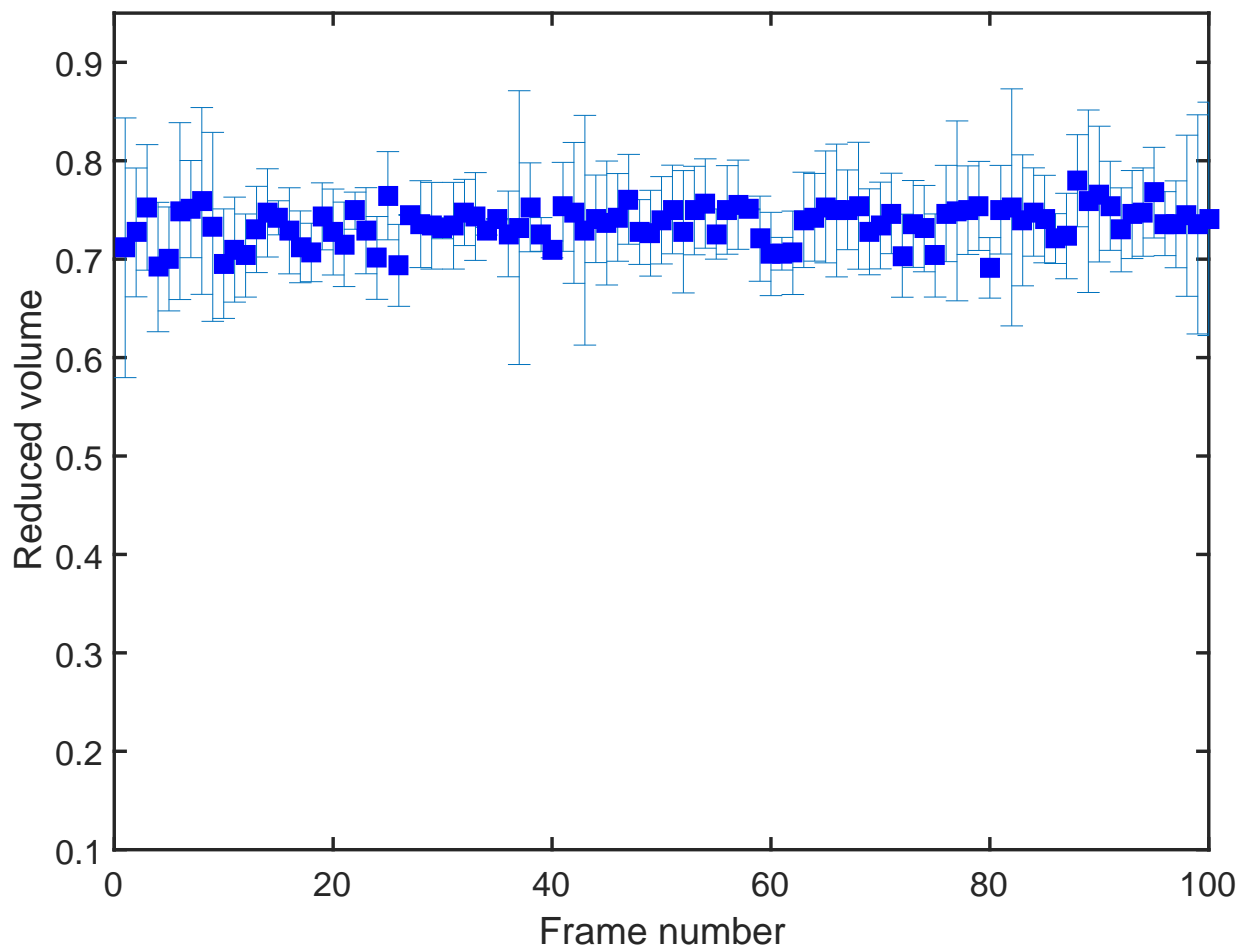
FIG. S4. Reduced volume as a function of frame number for the vesicle shown in Fig. S2. The reduced volume is determined to be $\nu = 0.735 \pm 0.0003$.

IV. BENDING MODULUS

Because our method for selecting vesicles for determination of bending modulus depends on a strict set of statistical rejection criteria (see Experimental Methods), our results show a relatively narrow distribution of vesicle bending moduli within an individual sample (green and blue bars in Fig. S5). However, our results show that the average bending modulus generally depends on the batch for vesicles prepared on different days (Fig. S5). We note that the same experimental electroformation protocol was used to prepare vesicles in the different batches. Differences in the average bending modulus may arise due to slight differences in handling (e.g. delivery into microfluidic devices) on different days. Nevertheless, the bending modulus values measured on different samples are consistent with prior work and lie in the same range to those reported in literature for DOPC vesicles [5, 9, 10].
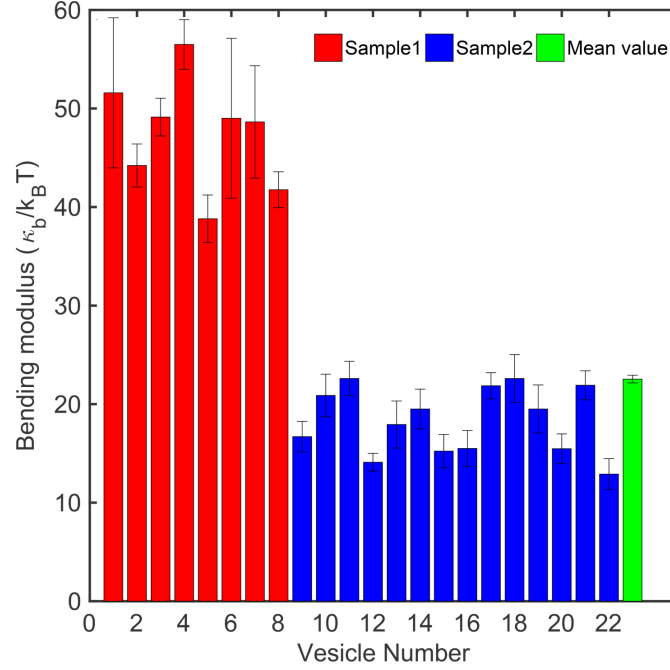

FIG. S5. Bending modulus measurements for individual vesicles on different samples shown in red and blue. The green bar shows the ensemble average value over $N = 22$ vesicles.

V.   SUPPLEMENTARY MOVIES

Movie S1

Movie of a tubular vesicle with initial reduced volume $\nu = 0.53$. This vesicle falls in the highly deflated regime (green symbols in Fig.5 in main text) of phase diagram. At $Ca = 2.3$, the tubular vesicle forms symmetric dumbbell and reaches a steady-state.

Movie S2

Movie of a spheroid vesicle with initial reduced volume $\nu = 0.73$. This vesicle falls in the moderately deflated regime (red symbols in Fig.5 in main text) of phase diagram. At $Ca = 98.7$, the vesicle forms asymmetric dumbbell and reaches a steady-state. Thermal fluctuations are visible on the vesicle boundary even under flow.

Movie S3

Movie of a quasi-spherical vesicle with initial reduced volume $\nu = 0.95$. This vesicle falls in the low deflated regime (magenta symbols in Fig. 5 in the main text) of phase diagram. Thermal fluctuations can be seen even under flow. The vesicle forms stable ellipsoid under flow and maintains this shape for a large range of Ca up to $Ca \approx 1000$.

---

[1] S. M. Anthony and S. Granick, *Langmuir*, 2009, **25**, 8152–8160.
[2] K. Chen, S. M. Anthony and S. Granick, *Langmuir*, 2014, **30**, 4760–4766.
[3] J. Pécréaux, H.-G. Döbereiner, J. Prost, J.-F. Joanny and P. Bassereau, *The European Physical Journal E: Soft Matter and Biological Physics*, 2004, **13**, 277–290.
[4] P. Shchelokovskyy, S. Tristram-Nagle and R. Dimova, *New journal of physics*, 2011, **13**, 025004.
[5] R. Dimova, *Advances in colloid and interface science*, 2014, **208**, 225–234.
[6] P. R. Bevington, D. K. Robinson, J. M. Blair, A. J. Mallinckrodt and S. McKay, *Computers in Physics*, 1993, **7**, 415–416.
[7] H. Zhou, B. B. Gabilondo, W. Losert and W. van de Water, *Physical Review E*, 2011, **83**, 011905.
[8] J. B. Dahl, V. Narsimhan, B. Gouveia, S. Kumar, E. S. Shaqfeh and S. J. Muller, *Soft matter*, 2016, **12**, 3787–3796.
[9] J. F. Nagle, M. S. Jablin and S. Tristram-Nagle, *Chemistry and physics of lipids*, 2016, **196**, 76–80.
[10] R. S. Gracià, N. Bezlyepkina, R. L. Knorr, R. Lipowsky and R. Dimova, *Soft Matter*, 2010, **6**, 1472–1482.